TRENDS IN SCIENCES 2026; 23(3): 11796
https://doi.org/10.48048/tis.2026.11796
RESEARCH ARTICLE

# Intercalation Engineering of MXene via Nickel Hydrothermal Treatment for Anti-Restacking and High-Stability Hybrid Supercapacitors

**Muhamad Subhan Septian[1,2], Ishmah Luthfiyah[3], Worawat Meevesana[3], Agus Purwanto[4], Agus Subagio[5], Harith Ahmad[6,7], Nida Usholihah[1,2] and Markus Diantoro[1,2,*]**

*[1]Department of Physics, Faculty of Mathematics and Natural Science, Universitas Negeri Malang, Malang 65145, Indonesia*
*[2]Center of Advanced Materials for Renewable Energy, Universitas Negeri Malang, Malang 65145, Indonesia*
*[3]School of Physics, Institute of Science, Suranaree University of Technology, Nakhon Ratchsima 30000, Thailand*
*[4]Department of Chemical Engineering, Faculty of Engineering, Universitas Negeri Sebelas Maret, Surakarta 57126, Indonesia*
*[5]Department of Physics, Faculty of Mathematics and Natural Sciences, Universitas Negeri Diponegoro, Semarang 50275, Indonesia*
*[6]Department of Physics, Faculty of Science, Universiti Malaya, Kuala Lumpur 50603, Malaysia*
*[7]Adjunct Professor, Department of Physics, Universitas Negeri Malang, Malang 65145, Indonesia*

**([*]Corresponding author's e-mail: markus.diantoro.fmipa@um.ac.id)**

*Received: 5 September 2025, Revised: 10 October 2025, Accepted: 15 October 2025, Published: 15 December 2025*

**Abstract**

Intercalation engineering of MXene via nickel hydrothermal treatment was investigated to improve interlayer spacing, prevent restacking, and enhance the electrochemical performance of hybrid supercapacitors. MXene was synthesized by etching the aluminum layer from the MAX phase, and nickel was successfully intercalated between the layers using a hydrothermal process. X-ray diffraction (XRD) analysis revealed an increase in d-spacing from 9.94 Å for pristine MXene to 13.01 Å for MXN2, confirming effective suppression of restacking. The specific surface area of MXN2 reached 35.27 $m^2$ $g^{-1}$, significantly higher than pristine MXene (3.96 $m^2$ $g^{-1}$). Electrochemical testing showed MXN2 achieved a specific capacitance of 118.9 F $g^{-1}$ in a 3-electrode system, and 60.03 F $g^{-1}$ in a 2-electrode coin cell, with an energy density of 6.48 Wh $kg^{-1}$ and excellent cycling stability (97.47% retention after 1,000 cycles). These findings demonstrate that nickel intercalation significantly enhances MXene's structural and electrochemical properties, making MXN2 a promising material for high-stability hybrid supercapacitors.

**Keywords:** MXene, Intercalation nickel (Ni), Self-restacking, Supercapacitor, Activated carbon

## Introduction

The International Energy Agency (IEA) predicts that the global renewable energy capacity will increase by nearly 3,700 GW between 2023 and 2028, with renewable sources expected to contribute more than 42% of global electricity production by the end of 2028 [1]. This anticipated growth in renewable energy necessitates the development of efficient energy storage systems that can effectively support various applications in sustainable energy [2]. Among these, supercapacitors have garnered significant attention due to their fast charge/discharge rates, exceptional cycle stability, environmental sustainability, and safety features [3,4]. Supercapacitors can be classified into 3 types based on their energy storage mechanisms: Electric Double-Layer Capacitors (EDLCs), pseudocapacitors, and

hybrid supercapacitors [5]. EDLCs operate through electrostatic interactions at the electrode surface, making them suitable for carbon-based materials. Pseudocapacitors, on the other hand, utilize faradaic processes and rely on materials such as conductive polymers and transition metal oxides for charge storage. Hybrid supercapacitors combine the characteristics of both EDLCs and pseudocapacitors, utilizing both mechanisms of energy storage to deliver superior performance [6].

MXenes, a family of 2-dimensional (2D) materials, have attracted significant attention as supercapacitor electrodes owing to their high hydrophilicity, tunable interlayer spacing, excellent electrical conductivity, and long cycle life [7,8]. These materials ($M_{n+1}X_nTx$) are commonly synthesized via selective etching of MAX phases (Mn + 1AXn). Among them, $Ti_3C_2Tx$ has been the most extensively studied, due to its remarkable conductivity (~15,000 S $cm^{-1}$), mechanical robustness, and superior electrochemical properties [9]. Despite these advantages, MXenes face intrinsic limitations arising from their 2D nanosheet architecture. The nanosheets tend to restack due to van der waals force in the surface termination group, leading to a reduced interlayer spacing that impedes ion transport and diminishes the accessible surface area for charge storage [10]. This structural restacking increases ion diffusion resistance, thereby restricting electrolyte accessibility and ultimately degrading the electrochemical performance of $Ti_3C_2Tx$ electrodes [11].

MXene composites with transitional metal materials are necessary to enhance redox reactions and improve capacitance [12]. Previous studies, such as those by Zhang *et al.* [13] demonstrated that the incorporating Ni composites into 3D porous MXene, achieving a specific capacitance of 85 F $g^{-1}$, which is higher than that of 3D porous MXene alone 67 F $g^{-1}$. However, these improvements are limited by the ongoing issue of MXene self-restacking, which reduces performance despite the use of transition metal composites [14]. To overcome this problem, the intercalation of nickel into MXene layers is required to prevent self-restacking. Das *et al.* [15] addressed this challenge by using silica ($SiO_2$) insertion into MXene layer, which resulted in a specific capacitance of 648 F $g^{-1}$, significantly higher than the pure MXene's specific capacitance of 246.6 F $g^{-1}$. Additionally, Lu *et al.* [16] investigated asymmetric devices using Co@MXene//AC electrodes, achieving a specific capacitance of 23.7 mAh $g^{-1}$ with an energy density of 19 Wh $kg^{-1}$ at a power density of 400 W $kg^{-1}$ [16].

Numerous studies have focused on the intercalation of transition metal (TM) materials into MXene interlayers. The amount of intercalated material is directly proportional to the quantity of transition metal precursor used. However, in most studies, the mass ratio of transition metal precursors used has been relatively high (MXene: TM = 1: > 0.5 wt/wt%), which results in the morphology of the MXene layers being fully covered by the intercalated metal material. Therefore, further research is needed to investigate the effect of using smaller quantities of transition metal precursors (MXene TR: TM = 1: < 0.2 wt/wt%) with the hydrothermal method, ensuring that the transition metal materials only intercalate into the MXene functional groups rather than adhering to the surface of MXene. Nickel is the preferred transition metal in this study because its ionization energy (737.1 kJ $mol^{-1}$) is lower than that of silicon (786.5 kJ $mol^{-1}$) and cobalt (760.4 kJ $mol^{-1}$), which have been used in previous research, making nickel intercalation easier. This study focuses on Intercalation Engineering of MXene via Nickel Hydrothermal Treatment to address the issue of self-restacking and to produce a high-stability hybrid structure for supercapacitors. The hydrothermal intercalation of Nickel into the MXene layers is expected to prevent restacking by enhancing the interlayer spacing, improving ion diffusion, and thus increasing the overall capacitance and electrochemical performance. The findings from this research aim to contribute to the advancement of high-performance supercapacitors, which are vital for the growing demand for efficient energy storage solutions in the renewable energy sector. The performance of the MXene-Ni-based electrode will be evaluated in a symmetric supercapacitor device using activated carbon, which is known for its high surface area, in the form of a coin cell. This approach is expected to contribute to the advancement of electrical energy storage technology.

Numerous studies have investigated the intercalation of transition metals (TMs) into MXene interlayers. The extent of intercalation is generally proportional to the amount of TM precursor used. In

most reports, however, relatively high precursor loadings are employed (MXene:TM ≥ 1:0.5 wt/wt%). This often leads to excessive deposition, where the MXene surface becomes fully covered rather than selectively intercalated. To overcome this limitation, it is necessary to examine lower precursor concentrations (MXene:TM ≤ 1:0.2 wt/wt%) under hydrothermal conditions. This approach favors intercalation into the MXene functional groups without unwanted surface coverage. Nickel was chosen as the transition metal due to its lower ionization energy (737.1 kJ $mol^{-1}$) compared with silicon (786.5 kJ $mol^{-1}$) and cobalt (760.4 kJ $mol^{-1}$), both reported in earlier studies. The lower ionization energy of nickel facilitates more efficient intercalation. In this work, we propose intercalation engineering of MXene via hydrothermal nickel treatment to mitigate self-restacking and create a structurally stable hybrid electrode. Nickel intercalation is expected to expand the MXene interlayer spacing, enhance ion transport, and improve electrochemical performance. The performance of the MXene–Ni hybrid electrode will be evaluated in a symmetric coin-cell supercapacitor using activated carbon as the counter electrode. Activated carbon was selected for its high surface area and proven reliability. This study aims to advance the development of efficient and stable energy storage devices for renewable energy technologies.

## Materials and methods

### Materials

The materials used in this study included titanium aluminum carbide ($Ti_3AlC_2$, 99% purity (200 mesh) Luoyang Tongrun Info Technology Co., Ltd, China) as the MAX phase, 48% hydrofluoric acid (HF, Sigma-Aldrich, China), nickel chloride hexahydrate ($NiCl_2 \cdot 6H_2O$,237.69 g/mol, Merck), cetyltrimethylam monium bromide (CTAB, purity 98%, Sigma Aldrich, China), urea ($(NH_2)_2CO$, Merck), activated carbon (CGC, Bangkok, Thailand) , carbon black (Imerys, La Hulpe, Belgium), N-methyl-2-pyrrolidone (NMP, Merck, Germany), polyvinylidene fluoride (PVDF, Sigma Aldrich, USA), aluminum foil substrate, a coin cell tool set (TOB Machine, Fujian, China), tetraethylammonium tetrafluoroborate ($Et_4NBF_4$, Gelon, Shandong, China) this ionic liquid electrolyte is known for its wide electrochemical stability window and high ionic conductivity, making it ideal for high-performance supercapacitors, sodium sulphate ($Na_2SO_4$, Merck, Germany), whatman paper as a separator, and deionized (DI) water. All the chemicals had analytical grade purity and were used as received without any purification.

### Materials for synthesis MXene

After the successful synthesis of the first layered $Ti_3C_2T_x$ using hydrofluoric acid, several other methods were developed and implemented to obtain various MXenes with new compositions. To date, there are 2 different strategies for obtaining MXenes using the "top-down" and "bottom-up" approaches (**Figure 1**) [17]. Top-Down Strategy: This approach involves selective etching, where the bulk MAX phase is broken down into individual MXene layers. Various etching agents are used, including acids like HF and $H_3PO_4$, alkalis like NaOH, fluoride salts with HCl (e.g., LiF + KF, $NH_4F$), and even molten salts like $NH_4HF_2$. The *top-down* method is highly effective in producing well-defined MXene layers due to the ability of these etchants, especially HF, to selectively remove the aluminum layer from the MAX phase, leaving behind the titanium and carbon layers to form the MXene structure. This method is efficient in creating the exfoliated structure but poses safety risks and scalability challenges, especially with HF. Bottom-Up Strategy: This involves chemical vapor deposition (CVD), where MXenes are synthesized layer by layer, starting from the atomic or molecular level. This method offers an alternative to the top-down approach, potentially avoiding the use of hazardous chemicals like HF. However, it presents its own set of challenges, including the control of material quality and scalability Hydrofluoric acid (HF) is highly effective because of its ability to break the strong bonds between the metal and carbon atoms in the MAX phase. It specifically etches the aluminum layer, allowing the remaining layers of titanium and carbon to form the MXene structure. HF's unique reactivity makes it highly efficient in creating the exfoliated structure with well-defined layers.

On the other hand, while alternatives like LiF/HCl can etch the MAX phase, they may not be as selective or efficient. LiF, for example, can react with the metal layer but might not provide the same precise etching necessary for producing high-quality MXenes with well-defined layered structures. The etching process

may be slower or less complete, resulting in poor exfoliation and lower-quality MXene layers. Additionally, without HF, the reaction might not generate the same level of ionic activity needed for successful delamination. Use of 48% HF in the synthesis method poses both safety concerns and challenges related to scalability. To address these issues, we will explore and discuss alternative synthesis methods that do not rely on HF. One promising alternative is the use of citric acid, which can effectively replace HF in certain synthesis processes while maintaining similar structural and electrochemical properties. Citric acid is non-toxic, more environmentally friendly, and easier to handle, making it a safer choice for large-scale production. Another alternative could be using phosphoric acid, which has similar properties to HF but is less hazardous and more widely accepted in industrial applications.

**Synthesis of MXene intercalated by nickel**

The synthesis of MXene was conducted by etching the aluminum layer from the MAX phase material. This process involved stirring 1 g of MAX material in 20 mL of 48% HF solution at room temperature for 24 h. After etching, the solution was washed with deionized (DI) water using a centrifuge at 4,000 rpm for 10 min until the pH of the solution reached approximately 6. Once the desired pH was achieved, the sample was separated from the solution, transferred to a petri dish, and dried at 100 °C for 1 h. $Ti_3C_2T_x$/NiThe intercalation of nickel (Ni) into the MXene was performed by mixing 1 g of MXene powder, 0.067 g of $NiCl_2{\cdot}6H_2O$, 0.23 g of CTAB, and 0.13 g of urea in 50 mL of DI water. The mixture was stirred for 30 min at room temperature until homogeneous and then transferred to a Teflon-lined autoclave, where it was heated at 160 °C for 8 h. The intercalation process was repeated for different $NiCl_2{\cdot}6H_2O$ mass variations: 0.067 g (MXN1), 0.1 g (MXN2), and 0.2 g (MXN3). The resulting solutions were washed 3 times with DI water and ethanol, followed by drying in an oven at 800 °C for 1 h. Finally, the samples were calcined at 550 °C for 2 h under a nitrogen atmosphere, following the flow diagram illustrated in **Figure 1**.

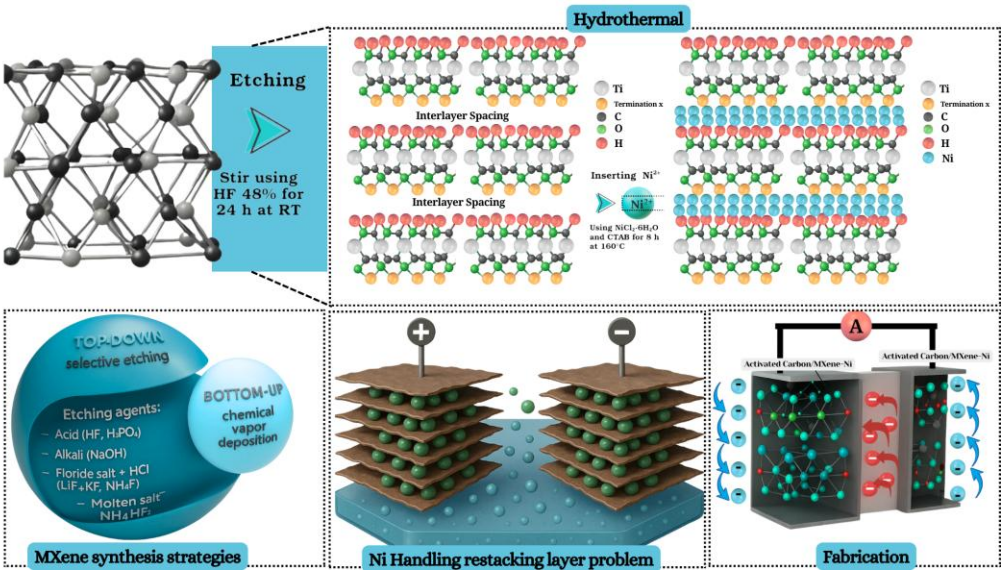


**Figure 1** Schematic Illustration of the synthesis of MXene/Ni from MAX Phase and the system of symmetrical supercapacitor.

**Material characterization**

The phases of the MAX, MXene, and MXene/Ni materials were characterized using a Bruker D8 Advance X-Ray Diffraction (XRD) system with Cu Kα radiation, operating in the 2θ range of 5° - 90°. Scanning Electron Microscopy (SEM) with an SU3500 instrument and Transmission Electron Microscopy (TEM) with an HT7700 instrument were used to observe the morphology of the synthesized materials. The Brunauer-Emmett-Teller (BET) method with a NOVA 2200e instrument was used to determine the specific surface area, based on nitrogen gas adsorption after degassing at

150 °C for 12 h. Raman spectroscopy was performed using a HORIBA LabRAM HR Evolution Raman microscope equipped with a 785 nm laser and a 600 g/mm grating.

**Fabrication of coin cell supercapacitor**

The fabrication of the supercapacitor coin cell began with preparing the electrodes. A mixture of AC/MXene-Ni as the active material, carbon black as the conductive agent, PVDF as the binder (in a weight ratio of 8:1:1), and NMP as the solvent was used. During the mixing process, the solution temperature was maintained at 80 °C to facilitate the dissolution of PVDF in NMP. The mixture was stirred for 8 h at 60 °C to ensure homogeneity. The resulting slurry was then applied to an aluminum foil substrate using a doctor blade and dried at 80 °C for 2 h. Finally, the electrodes were assembled into coin cells with a 1 M $Et_4NBF_4$ electrolyte and a whatman paper separator, arranged symmetrically.

**Electrochemical measurements**

Electrochemical measurements of the fabricated coin cells were conducted, focusing on galvanostatic charge-discharge (GCD) performance. The specific capacitance ($C_s$) of the electrodes was calculated using Eq. (1) [18].

$$C_s = 4\frac{I.\Delta t}{m.\Delta V} \quad (1)$$

Then, the specific energy ($E_s$) and specific power ($P_s$) were determined using Eqs. (2) and (3) [19].

$$E_s = \frac{C_S(\Delta V)^2}{3{,}6} \times \frac{1}{2} \quad (2)$$

$$P_s = \frac{E_s}{\Delta t} \times 3{,}600 \quad (3)$$

where $I$ is the applied current (A), $\Delta t$ is the total discharge time (s), $m$ is the electrode mass (g), and $\Delta V$ is the potential difference during the discharge phase (V). The GCD test was performed over 1,000 cycles to determine the capacitance retention ($C_R$), calculated using Eq. (4).

$$C_R = \frac{C_{s(n)}}{C_{s(max)}} \times 100\% \quad (4)$$

$C_{s(n)}$ represents the specific capacitance at the n-$^{th}$ cycle (F $g^{-1}$), and $C_{s(max)}$ is the maximum specific capacitance achieved during the 1,000 cycles (F $g^{-1}$). For electrochemical impedance spectroscopy (EIS) and cyclic voltammetry (CV) measurements, a 3-electrode system was employed. In this setup, the AC/MXene-Ni functioned as the working electrode, while a platinum wire and Ag/AgCl were used as the counter and reference electrodes, respectively, with 1 M $Na_2SO_4$ serving as the electrolyte. From the CV curves, the specific capacitance of the material was calculated using Eq. (5) [20].

$$C_s = \frac{\int_{V_i}^{V_f} I(V)dV}{mv(V_f - V_i)} \times 1{,}000 \quad (5)$$

where $\int_{V_i}^{V_f} I(V)\,dV$ is the total area under the CV curve (A V), $m$ is the active material mass (g), $v$ is the scan rate ($mVs^{-1}$), and $V_f, V_i$ are the upper and lower limits of the potential window (V).

## Results and discussion

**Microstructural analysis**

The microstructural evolution of the synthesized samples was systematically investigated through X-ray Diffraction (XRD) to identify the crystalline phases present. Theoretically, the transformation from the MAX phase to MXene involves the selective etching of the 'A' layer (e.g., Al), which should result in a loss of corresponding diffraction peaks and a shift in others due to changes in interlayer spacing and the introduction of functional groups. As shown in **Figure 2(a)**, the diffraction pattern of the MAX phase confirms its crystalline nature, with characteristic peaks observed at 2θ = 9.44°, 19.01°, 38.61°, and 60.05°, corresponding to the (002), (004), (104), and (110) planes, respectively. Following the etching of the aluminum layer using 48% HF acid to form MXene, a critical change is observed: the complete disappearance of the (104) peak at 38.61°. This is a fundamental indicator of successful etching, as this peak is intrinsically linked to the presence of the aluminum layer in the MAX structure. Its absence confirms the effective removal of Al and the formation of MXene [21]. Furthermore, and of significant importance, the (002) peak - which is highly sensitive to interlayer spacing - shifts from 9.44° in the

MAX phase to a lower angle of 8.89° in the MXene phase. According to Bragg's law ($n\lambda = 2d \sin\theta$), a decrease in the diffraction angle ($2\theta$) signifies an increase in the interlayer d-spacing. This expansion is a direct consequence of the aluminum atoms being replaced by void spaces that are subsequently terminated with functional groups such as hydroxyl (-OH), oxygen (-O), and fluorine (-F), introduced during the etching and subsequent washing with deionized water ($H_2O$) [22].

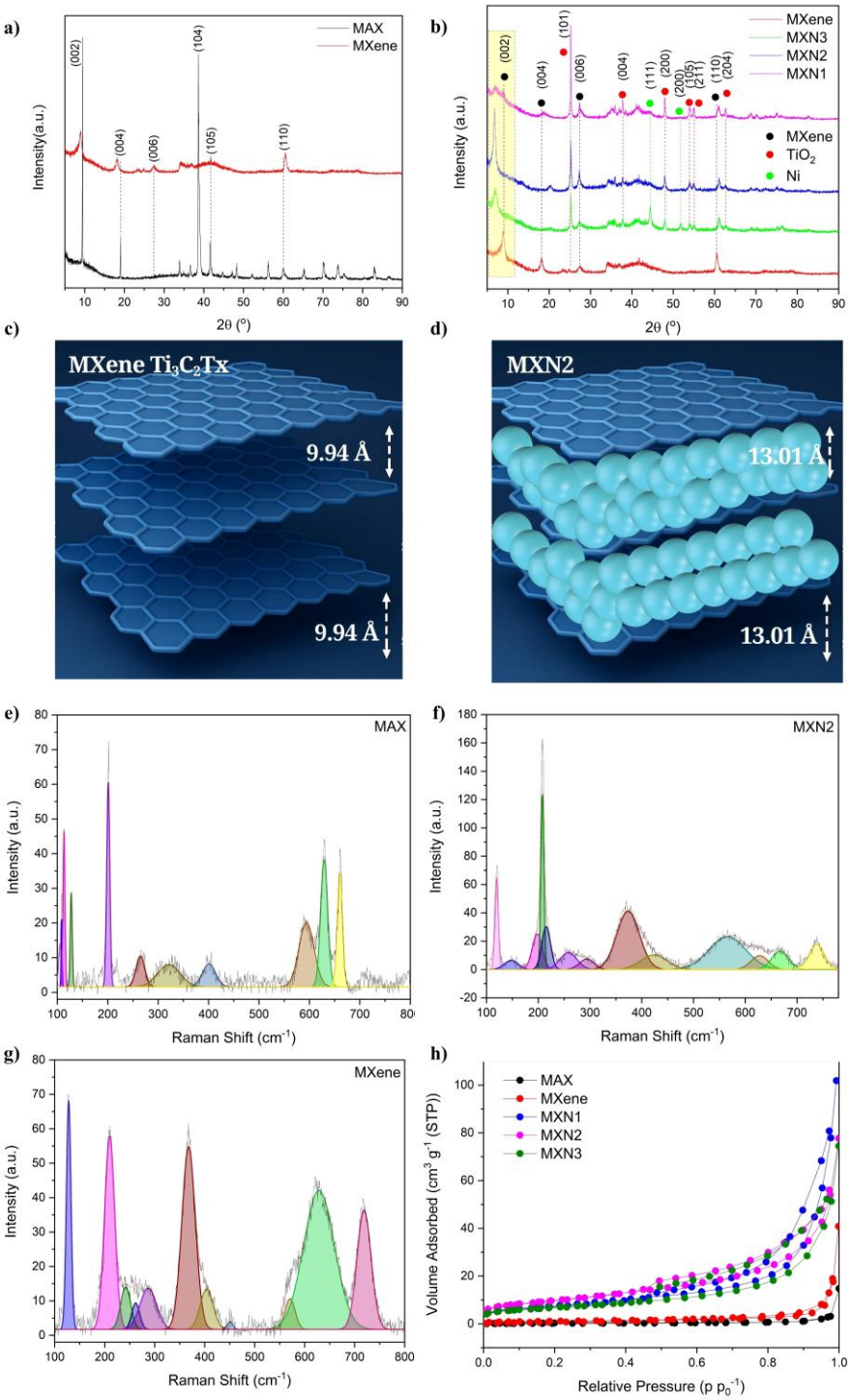


**Figure 2** (a) X-ray Diffraction (XRD) Patterns of MAX and MXene Phases, (b) XRD Patterns of Different MXene-Ni Variants (MXN1, MXN2, MXN3), (c) Illustration of the Interlayer Spacing in $Ti_3C_2Tx$ MXene, (d) Illustration of the Interlayer Spacing in MXN2, (e) Raman Spectra of MAX, (f) Raman Spectra of MXN2, (g) Raman Spectra of MXene, (h) Nitrogen Adsorption Isotherms (BET-BJH) for all variants.

**Figure 2(b)** presents the XRD patterns of the nickel-intercalated MXene samples (MXN1, MXN2 and MXN3). All samples retain the primary MXene characteristics; however, the MXN1 pattern exhibits additional peaks at 44.5° and 53°, identified as the (111) and (200) planes of a secondary nickel-containing phase. This is attributed to an excessive concentration of the nickel precursor in the MXN1 synthesis. Under hydrothermal conditions, the surplus $Ni^{2+}$ ions not only intercalate into MXene but also undergo hydrolysis with urea and water, precipitating as $Ni(OH)_2$ according to the reaction [23]. This is attributed to the excessive $Ni^{2+}$ ions reacting with oxygen and urea, leading to nickel hydrolysis during the hydrothermal process, as represented by the given reaction equation [24]. Each curve corresponds to a different MXene variant, with the characteristic diffraction peaks representing the crystal structure of each phase [25-32]. The comparison reveals changes in peak intensity and positions, suggesting variations in crystallinity, phase composition, and metal content in the MXene structures. These shifts are indicative of the impact of adding nickel (Ni) and other elements, influencing the material's overall structural integrity and potential applications.

$$Ni^{2+} + 4(NH_2)_2CO + 10H_2O \rightarrow 8(NH_4)^+ + Ni(OH)_2 + 2(HCO_3)^- + 2(CO_3)^{2-}$$

A key finding across the intercalated samples is the systematic shift of the (002) peak. The diffraction angle for this peak shifts to 6.82° for MXN1, 6.79° for MXN2, and 7° for MXN3. This indicates a further increase in d-spacing compared to pure MXene, with MXN2 exhibiting the largest expansion. This suggests that MXN2 achieved the most effective intercalation of nickel species, optimally widening the galleries without causing excessive phase segregation or disorder, as seen in MXN1. These peak shifts correlate directly with changes in d-spacing, where larger shifts indicate greater interlayer distances [15,33]. **Figure 2(c)** presents the interlayer spacing (d-Interlayer Spacing) calculations for various stages of MXene formation, with nickel (Ni) substitution. Initially, the MAX phase exhibits an interlayer spacing of 9.36 Å, reflecting the distance between the layers in the pristine MAX phase. This represents a typical interlayer distance for materials in the MAX phase, where the atomic layers are relatively close due to the presence of intercalating elements such as aluminum (Al). Upon etching to form MXene, the interlayer spacing increases to 9.94 Å, indicating the removal of Al atoms and the expansion of the interlayer distance. This change is typical for MXene materials, where the removal of certain elements results in the increased separation of the remaining layers.When Ni is introduced as a substitute in the MXene structure, a more substantial increase in interlayer spacing occurs. In the MXN1 phase, the interlayer spacing rises dramatically to 12.95 Å (**Figure 2(d)**), highlighting the influence of nickel substitution on the material's structural expansion. This increase in spacing is a result of the larger ionic radius of Ni compared to Al, which facilitates greater separation between the layers. In MXN2, the interlayer spacing slightly increases further to 13.01 Å, demonstrating continued expansion due to the ongoing substitution process. However, in MXN3, the interlayer spacing slightly decreases to 12.02 Å. This reduction could be attributed to structural reorganization or changes in the interaction between the nickel atoms and the MXene layers during further processing. Overall, these observations are consistent with the theory of metal-substituted MXenes, where metal ions like Ni influence the structural characteristics of MXene, including the interlayer distance. The increasing interlayer spacing is indicative of enhanced exfoliation and potential for improved properties such as electrical conductivity, which are vital for applications in energy storage and other technological uses. The variations in spacing, particularly the decrease in MXN3, reflect the complex interplay between metal substitution and the structural dynamics of MXenes. Variations in the crystallinity and phase composition are also evident from the peak intensities. The (002) peak in MXN1 appears broadened and less intense, indicating a more disordered or amorphous structure. Concurrently, all intercalated samples exhibit the emergence of diffraction peaks attributable to $TiO_2$ (e.g., at 25.42° (101) and 37.78° (004)), confirming the partial oxidation of the MXene Ti layers during the hydrothermal process. This is confirmed by the appearance of $TiO_2$ diffraction peaks at the (101), (004), (200), (105), (211), and (204) planes, corresponding to angles of 25.42°, 37.78°, 48.00°, 54.00°, 55.00°, and 62.65°, respectively [34]. The intensity of the $TiO_2$ (101) peak is most pronounced in

MXN3, suggesting a higher degree of oxidation. This is consistent with a higher initial MXene content in MXN3, which provides a larger reactive surface area for conversion to $TiO_2$. Furthermore, the intensity of the (101) peak differs across variations, with MXN1 showing a higher intensity compared to MXN2 and MXN1. This is because the MXN1 sample contains a higher amount of MXene, resulting in a greater surface area being converted into $TiO_2$ during the hydrothermal process compared to the other variations [35]. Consequently, MXN2 shows the highest interlayer distance compared to the other variations. To determine the bonding in the synthesized material structures, lattice vibrations in the wavenumber range of 100 - 800 $cm^{-1}$ were analyzed. The Raman spectra of MAX and MXene are divided into 3 main regions: the flake region, associated with vibrations of carbon groups, 2 titanium layers, and surface groups; the Tx region, representing the vibrations of surface groups; and the C region, corresponding to the vibrations of carbon atoms. The vibrations in MAX and MXene consist of 2 primary modes: in-plane (Eg) and out-of-plane (Ag), which involve the outer layer, carbon, and surface groups [36].

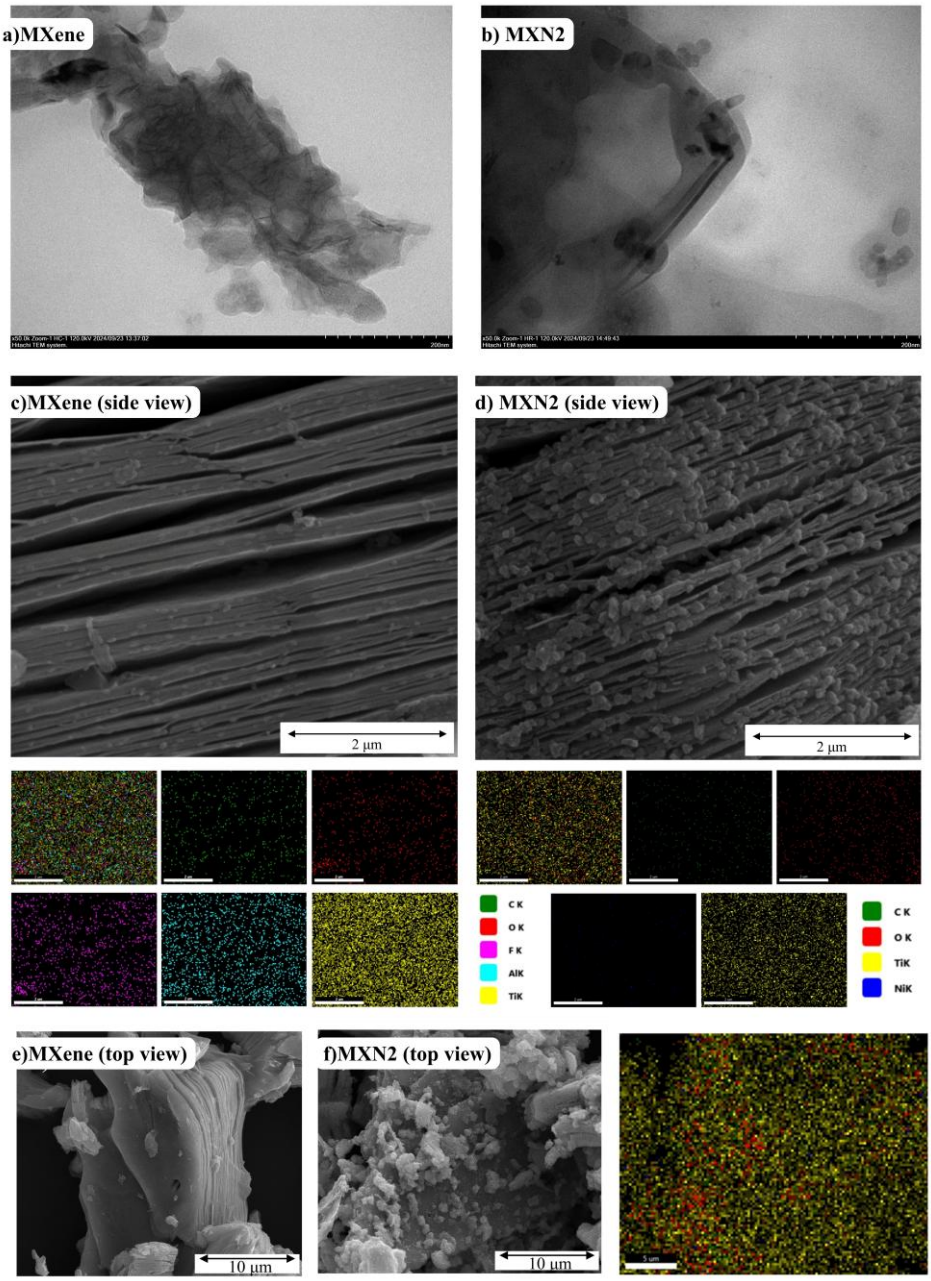


**Figure 3** Element analysis TEM image of (a) MXene and (b) MXN2, SEM EDX Mapping of (c) MXene, (d) MXN2 (side view), (e) MXene and (f) MXN2 (top view).

**Figures 2(e) - 2(g)** presents the Raman spectra for MAX, MXene, and MXN2, with key peaks observed in the ranges of 100 - 250 $cm^{-1}$ for the flake region, 230 - 500 $cm^{-1}$ for the Tx region, and 550 - 800 $cm^{-1}$ for the C region [37]. The MAX phase is shown, which lacks the characteristic accordion-like morphology of MXene. This structure is still intact because the aluminum (Al) layer has not been removed. As a result, the MAX phase maintains its compact, non-exfoliated form, indicating that the aluminum is still part of the structure and contributes to its layered arrangement. In this phase, the Ti-Al bonds are stronger, which is reflected in the peak ranges seen in the vibrational spectra (105 - 113 $cm^{-1}$), confirming the intact bonding between Ti and Al. In the flake region of MAX, peaks in the 105 - 113 $cm^{-1}$ range represent strong bonds between Ti and Al; however, these peaks disappear in MXene due to the exfoliation of Al. Furthermore, the Tx region of MXene shows increased intensity and full width at half maximum (FWHM) compared to MAX, indicating a higher concentration of surface groups on the MXene surface. In the C region, the increased intensity and FWHM suggest strengthened Ti-C bonds due to the absence of Al. In the flake region of MXN2, a peak at 148 $cm^{-1}$ corresponds to Ti-O bonding. The specific surface area of the materials was determined using the BET method. The results show that MXN2 has the highest specific surface area of 35.27 $m^2\ g^{-1}$, compared to MXN1, MXN3, pure MXene, and MAX, which have specific surface areas of 24.06, 27.1, 3.96 and 1.1 $m^2\ g^{-1}$, respectively. There is a significant difference in specific surface area between MAX, pure MXene, and the samples with variations. The $N_2$ adsorption-desorption isotherms also exhibit distinct behavior, as shown in **Figure 2(h)**. The isotherms for MAX and pure MXene correspond to type III curves according to IUPAC classification, indicating very weak interactions between the adsorbate and the adsorbent surface. In contrast, the isotherms for the sample variations correspond to type IV H3 curves, as evident from the hysteresis loops. This indicates that the particles formed in these samples have a plate-like, stacked structure, resembling an accordion. Additionally, for all sample variations, there is a slight curvature in the region $0 < p/p_0 < 0.1$. This suggests some interaction between the adsorbate and the adsorbent surface, facilitating electrolyte adsorption and enhancing the material's suitability for energy storage applications. and reference electrodes. Additionally, a peak at 209 $cm^{-1}$ with higher intensity than in MXene is associated with out-of-plane vibrations of Ti-O, caused by enhanced interlayer coupling due to Ni ions and expanded interlayer distance. In the Tx region, the intensity for MXN2 is lower than for MXene, reflecting a reduction in surface groups due to the presence of $TiO_2$ and nickel, as confirmed by XRD results. In the C region, MXene exhibits a peak at 719 $cm^{-1}$, representing in-plane stretching of Ti-C. This peak shifts to 738 $cm^{-1}$ in MXN2, indicating strengthened Ti-C bonds resulting from nickel intercalation.

In **Figure 3(a)**, This transmission electron microscope (TEM) image shows the morphology of MXene, revealing its layered structure. The dark areas indicate regions of the sample, with visible sheets of MXene, which are essential for its properties like high conductivity and surface reactivity [38-40]. **Figure 3(b)** Similar to the previous image, this is a TEM image of MXN2, but it shows a different material composition. The elongated and distinct shapes suggest variations in the structural form of MXN2 compared to MXene, possibly resulting from modifications in its synthesis process. **Figures 3(a)** and **3(b)** represents TEM images highlighting differences between MXene and MXN2. Notably, MXN2 exhibits numerous small black spherical spots, corresponding to $TiO_2$ and Ni. The microstructure of the material was further analyzed using SEM, as shown in **Figures 3(c)** and **3(d)**, the MAX phase exhibits a structure that lacks the characteristic accordion-like morphology, as the aluminum layer is still present. In contrast, **Figure 3(c)** shows that the MXene phase adopts an accordion-like structure due to the removal of the aluminum layer, which is replaced by functional groups formed within the layers. The elevated temperature and pressure conditions of the hydrothermal process facilitate a more uniform intercalation of Ni within the MXene interlayers [41]. As shown in **Figures 3(c)** and **3(d)**, a substantial and well-distributed population of Ni particles is present between the MXene layers, with MXN3 exhibiting a higher density of Ni particles than MXN2 and MXN1 (**Figures 3(c) - 3(f)**).

Ni intercalation is evident in all variations; however, MXN2 (**Figure 3(d)**) demonstrates the most pronounced incorporation of Ni within the interlayers. In addition, a $TiO_2$ phase is detected on the surface of the MXene sheets. While pure MXene (**Figure 3(f)**) contains no $TiO_2$, the emergence of $TiO_2$ particles is clearly observed in **Figures 3(c)** and **3(d)**, with their abundance increasing progressively from MXN3 to MXN1. Notably, MXN3 (**Figures 3(d)** and **3(e)**) exhibits the highest concentration of $TiO_2$ particles, indicating a more extensive conversion of MXene to $TiO_2$ in this sample.

**Figures 3(c) - 3(f)** shows the SEM-EDX mapping of MXN2 from side and top views. **Figures 3(c) - 3(f)** represents the side view SEM-EDX of MXene, revealing the presence of Al and F in the sample. Meanwhile, **Figures 3(c) - 3(f)** displays spherical materials attached to the MXene layers, identified as Ni and TiO, with no Al or F remaining due to the hydrothermal process. Additionally, **Figure 3(f)** shows the top view of MXene, which has a smooth surface without any attached materials. In contrast, **Figure 3(f)**, depicting the top view of MXN2, reveals numerous materials rich in oxygen, identified as $TiO_2$. This observation aligns with the XRD results, which show a significant $TiO_2$ peak. The EDX data for MXene and MXN2 are summarized in **Table 1**.

**Table 1** EDX of MXene and MXN2.

| Materials | Ti (%At) | C (%At) | O (%At) | Al (%At) | F (%At) | Ni (%At) |
|---|---|---|---|---|---|---|
| MXene | 22.7 | 35.2 | 19.1 | 4 | 19.1 | - |
| MXN2 (Side) | 18.7 | 38.6 | 41.2 | - | - | 1.5 |
| MXN2 (top) | 29.9 | 27 | 42.3 | - | - | 0.8 |

This observation aligns with the XRD results, which show a significant $TiO_2$ peak. The EDX data for MXene and MXN2 are summarized in **Table 1**. **Figures 3(a)** and **3(b)** represents TEM images highlighting differences between MXene and MXN2. Notably, MXN2 exhibits numerous small black spherical spots, corresponding to $TiO_2$ and Ni. The structural and elemental analysis presented in these figures highlights the significant differences between MAX, MXene, and MXN2. The exfoliation of aluminum in MXene leads to an accordion-like structure that enhances surface functionality, while Ni intercalation and $TiO_2$ formation in MXN2 further modify the material's properties, increasing its surface area and enhancing its suitability for energy-related applications.

**Electrochemical performances**

The CV curves in panel **Figure 4(a)** show the electrochemical behavior of the supercapacitor electrodes at a scan rate of 10 mV $s^{-1}$. The electrodes are composed of various materials: AC/MAX, AC/MXene, AC/MXN1, AC/MXN2, and AC/MXN3. AC/MAX shows a typical double-layer capacitance behavior, with a rectangular shape, which indicates good ionic movement and charge storage at the electrode-electrolyte interface. AC/MXene shows a similar trend but with a slightly more pronounced peak current, suggesting that the MXene addition enhances the capacitive performance by offering more surface area for charge accumulation. AC/MXN1, AC/MXN2, and AC/MXN3 show broader peaks, indicating pseudocapacitance behavior, which is characteristic of the metal ions or functional groups in these samples (Ni in the interlayer of MXN1, MXN2, and MXN3), facilitating more reversible charge storage mechanisms. These curves provide insight into how MXene and its derivatives (with Ni intercalation) modify the electrochemical properties compared to the original AC/MAX material.

The supercapacitor behavior of the synthesized AC/MXene-Ni material, compared with AC/MAX and pure AC/MXene, is analyzed through cyclic voltammetry (CV) using a 1 M $Na_2SO_4$ electrolyte in a 3-electrode system. The synthesized material serves as the working electrode, while a platinum wire and Ag/AgCl were used as the counter

**Figure 4(a)** presents the CV results for all materials at a scan rate of 10 mV $s^{-1}$, with the gravimetric specific capacitance ($C_s$) for AC/MAX, AC/MXene, AC/MXN1, AC/MXN2, and AC/MXN3 being 27.9, 35.66, 55.79,

96.37 and 77.23 F $g^{-1}$, respectively. The CV graph for AC/MXene shows distinct behaviors during the charge process: From 0 to 0.5 V, the material exhibits EDLCs-like properties, while from 0.5 to 1 V, faradaic battery properties are observed. This dual behavior arises from the combination of AC as the EDLC (electric double-layer capacitor) component and MXene as the battery component in a symmetric supercapacitor configuration. During the discharge process of the AC/MXene sample, the material demonstrates battery-like behavior across the entire voltage range.

**Figure 4(b)** AC/MXN2 at different scan rates (2 to 10 mV $s^{-1}$). As the scan rate increases, the CV curve shifts, and the current density increases. This trend indicates that AC/MXN2 demonstrates good rate capability and fast charge-discharge behavior. The gradual increase in current with higher scan rates suggests a higher electrochemical activity and faster electron transfer, which is favorable for energy storage applications. Additionally, the curves remain nearly rectangular, confirming the excellent capacitive behavior of AC/MXN2 at varying scan rates. This behavior can be attributed to the abundance of functional groups in MXene, which facilitate faradaic reactions. In these reactions, the anode releases electrons that are subsequently accepted by the cathode, imparting battery-type characteristics to all discharge processes [42]. During the charging process of the AC/MAX, AC/MXN1, AC/MXN2, and AC/MXN3 samples, a similar trend to AC/MXene is observed. However, distinct differences emerge in the faradaic reaction process within the potential range of 0.5 - 1.0 V. Among these, AC/MXN3 exhibits superior faradaic activity, which can be ascribed to its higher Nickel content. The increased Nickel concentration enhances the specific surface area and promotes more efficient ion diffusion [43]. Nevertheless, excessive Ni loading can hinder ion transport pathways, as confirmed by the observed morphology. As a result, MXN2 demonstrates higher specific capacitance compared to MXN1 and MXN3. During the discharge process, all samples - except AC/MXene - exhibit behavior consistent with the electric double-layer capacitance (EDLC) of activated carbon (AC). The cyclic voltammetry (CV) profiles of MXN2 at scan rates ranging from 2 to 10 mV $s^{-1}$ are presented in **Figure 4(b)**. The corresponding specific capacitances are 118.9, 111.75, 103.82, 99.75, and 96.37 F $g^{-1}$ at 2, 4, 6, 8, and 10 mV $s^{-1}$, respectively. These results confirm that lower scan rates yield higher capacitance values. **Figure 4(c)** shows the specific capacitance for each material at different scan rates. As the scan rate increases, the specific capacitance decreases slightly, which is typical of capacitor-type materials. AC/MXN2 has the highest capacitance at lower scan rates, indicating superior charge storage capacity compared to other variants. **Figure 4(d)** Specific capacitance (F $g^{-1}$) for MAX, MXene, and MXN1 to MXN3 bar graph compares the specific capacitance for each material (MAX, MXene and the MXN series). The AC/MXN2 shows the highest specific capacitance, suggesting its excellent performance as an electrode material for supercapacitors or energy storage devices.

**Table 2** Specific capacitance, specific energy, and power density of coin cell supercapacitor.

| Materials | $C_s$ (F $g^{-1}$) | $E_s$ (Wh $kg^{-1}$) | $P_s$ (W $kg^{-1}$) |
|---|---|---|---|
| AC/MAX | 24.06 | 2.62 | 178.26 |
| AC/MXene | 31.57 | 3.36 | 177.76 |
| AC/MXN1 | 34.64 | 3.80 | 177.96 |
| AC/MXN2 | 60.03 | 6.48 | 176.72 |
| AC/MXN3 | 44.71 | 4.78 | 176.22 |

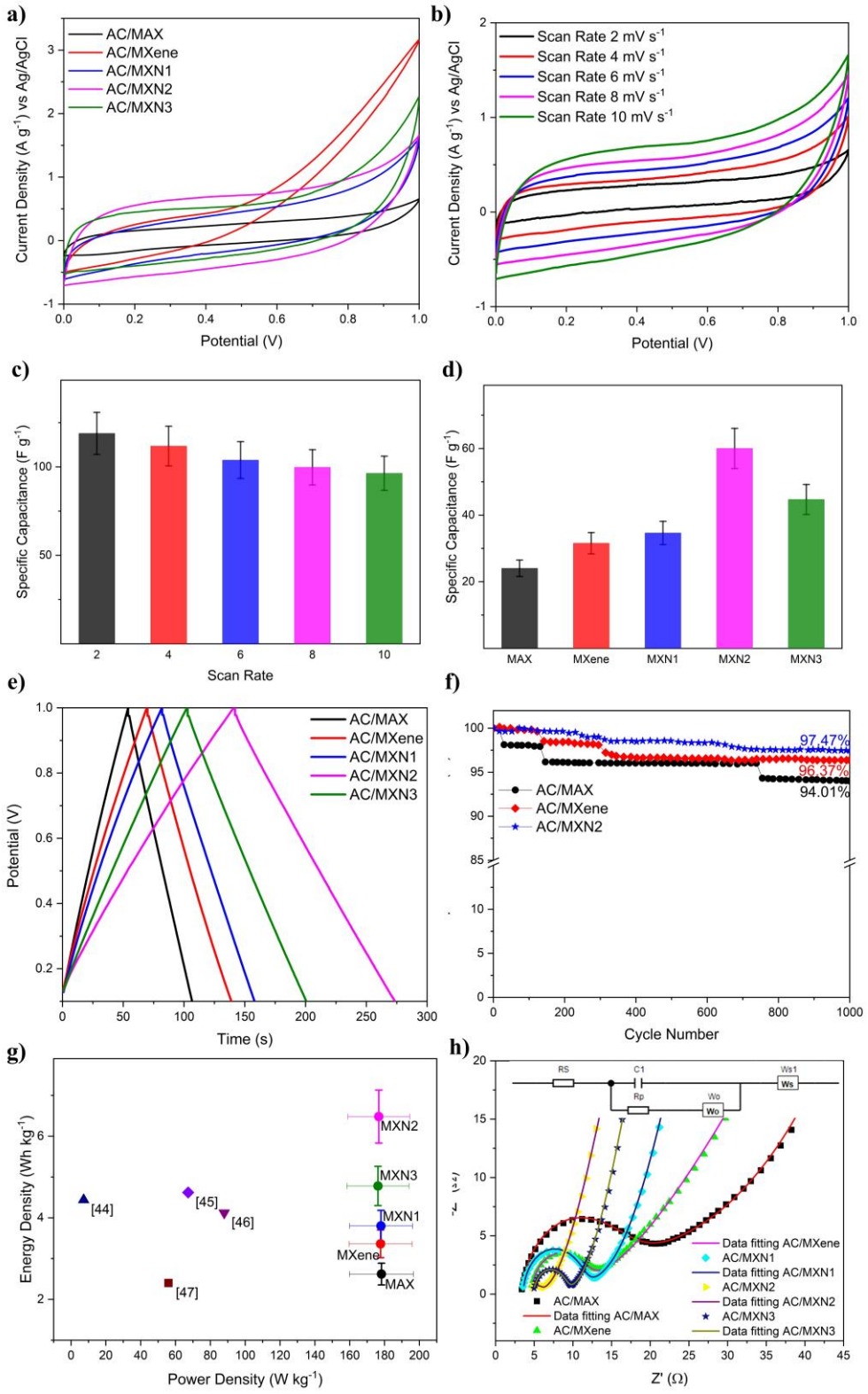


**Figure** 4 (a) CV curves of AC/MAX, AC/MXene, AC/MXN1, AC/MXN2, AC/MXN3 at a scan rate of 10 mV $s^{-1}$, (b) CV curves of AC/MXN2 at various scan rates, (c) illustration of the specific capacitance of AC/MXN2 at various scan rates, (d) illustration of the specific capacitance of each sample at a scan rate of 10 mV $s^{-1}$ (e) graph curves of AC/MXN2, d), AC/MXene, AC/MXN1, AC/MXN2, and AC/MXN3 at a current density of 0.1 A $g^{-1}$, and (f) capacitance retention graphs for MXN2 and MXene, (g) comparative Ragone plot illustrating the specific energy density (Wh $kg^{-1}$) versus power density (W $kg^{-1}$) of MXene-AC-Ni-based supercapacitor electrodes, and (h) Nyquist plot of AC/MAX, AC/MXene, AC/MXN1, AC/MXN2, and AC/MXN3.

The GCD (Galvanostatic Charge-Discharge) test was conducted using a coin cell supercapacitor device. The coin cell consisted of an electrode-separator whatman paper-electrode configuration, using 1 M $ET_4NBF_4$ as the electrolyte. The GCD curves at a current density of 0.1 A $g^{-1}$ for AC/MAX, AC/MXene, AC/MXN1, AC/MXN2, and AC/MXN3 are shown in **Figure 4(e)**. The discharge times of the AC/MXN1, AC/MXN2, and AC/MXN3 samples are longer compared to AC/MXene and AC/MAX. Among the modified samples, AC/MXN2 exhibits the longest discharge time. This result can be attributed to the optimal composition of Ni located between the MXene layers, which enhances the specific surface area and ion diffusion, making it superior to the other modified samples. Furthermore, AC/MXN2 also demonstrates the highest specific capacitance of 60.03 F $g^{-1}$, compared to AC/MAX, AC/MXene, AC/MXN1, and AC/MXN3, which exhibit specific capacitance of 24.06, 31.57, 34.64 and 44.71 F $g^{-1}$, respectively. The corresponding specific energy ($E_s$) and power density ($P_s$) values are summarized in **Table 2**. **Figure 4(f)** illustrates the capacitance retention of the coin cell supercapacitor for AC/MXene and AC/MXN2 after 1,000 cycles at a current density of 0.1 A $g^{-1}$. The capacitance retention of AC/MXN2 is higher at 97.47% compared to AC/MAX and AC/MXene, which retain only 94.01% and 96.37%. The retention of AC/MXN2 is higher due to its lower $R_{ct}$ compared to the other samples. Furthermore, the comparative Ragone plot in **Figure 4(g)** illustrates the relationship between specific energy density (Wh $kg^{-1}$) and power density (W $kg^{-1}$) for MXene-AC-Ni-based electrodes [44-47]. The performance of AC/MXN2 surpasses that of many previously reported systems, both in 3-electrode and practical 2-electrode configurations, as summarized in**Table 3**.

**Table 3** Comparison of electrochemical performance of the present word with other MXene-AC-Ni-based electrodes reported in the literature.

| Materials | Cs (F $g^{-1}$) | | Stability (Cycles) | Ref. |
|---|---|---|---|---|
| | 3 electrodes | 2 electrodes | | |
| $Ti_3C_2Tx$ ionogel film | 70 at 20 mV $s^{-1}$ | - | 90% at 20 mV $s^{-1}$ (1,000) | [43] |
| $Ti_3C_2Tx$/GDY-NTs | 63.7 at 10 mV $s^{-1}$ | - | 88.2% at 8 A $g^{-1}$ (10,000) | [48] |
| $Mo_{1.33}CTx$//NAC | 22 at 5 mV $s^{-1}$ | - | 97% at 100 mV $s^{-1}$ (5,000) | [49] |
| $Ti_3C_2Tx$/AC/TEAPW12 | 87 at 1 mV $s^{-1}$ | - | 102% at 1 mV $s^{-1}$ (10,000) | [50] |
| CF/$Ti_3C_2Tx$ | 100 at 10 mV $s^{-1}$ | - | 85% at 8 A $g^{-1}$ (2,000) | [51] |
| $Ti_3C_2Tx$/$Fe_3O_4$/RGO | - | 35.6 at 0.2 A $g^{-1}$ | 82.1% at 5 A $g^{-1}$ (5,000) | [52] |
| $Ti_3C_2Tx$/CNTs | - | 55.3 at 0.5 A $g^{-1}$ | - | [53] |
| CC/ $Ti_3C_2Tx$-$MnO_2$-CoNiLDHs//CC/AC | - | 45 at 0.5 A $g^{-1}$ | 79% at 2 A $g^{-1}$ (4,000) | [54] |
| $NiCo_2S_4$//$Ti_3C_2Tx$ | - | 54.57 at 2 A $g^{-1}$ | 79% at 30 A $g^{-1}$ (5,000) | [55] |
| $Ti_3C_2Tx$-Ni/AC | 118.9 at 2 mV $s^{-1}$ | 60.03 at 0.1 A $g^{-1}$ | 97.47% at 0.1 A $g^{-1}$ (1,000) | this work |

**Figure 4(h)** represent Nyquist plots from the EIS measurements conducted using a 3-electrode system, similar to the CV setup. Two key elements can be determined from the Nyquist plots: $R_s$ and $R_{ct}$. $R_s$ represents the resistance of the electrolyte solution and the testing cables, while $R_{ct}$ represents the charge transfer resistance at the interface between the electrode and the electrolyte. The $R_s$ and $R_{ct}$ for the AC/MXN2 sample are the lowest, measured at 4.55 and 1.04 Ω, respectively, compared to the other samples: AC/MAX (3.56 and 7.43 Ω), AC/MXene (4.70 and 5.22 Ω), AC/MXN1 (3.60 and 6.55 Ω), and AC/MXN3 (4.95 and

3.56 Ω). Further details can be found in **Table 4**. The smaller semicircle in the Nyquist plot for AC/MXN2 indicates superior facilitation of electrolyte ion penetration and diffusion within the electrode compared to the other samples.

**Table 4** Parameter of Nyquist plot.

| Materials | $R_s$ (Ω) | $R_{ct}$ (Ω) | $C$ ($\mu F$) |
|---|---|---|---|
| AC/MAX | 3.56 | 7.43 | 3.63 |
| AC/MXene | 4.70 | 5.22 | 3.48 |
| AC/MXN1 | 3.60 | 6.55 | 4.25 |
| AC/MXN2 | 4.55 | 1.04 | 29.52 |
| AC/MXN3 | 4.95 | 3.56 | 8.26 |

## Conclusions

The synthesis of MXene was successfully achieved through selective etching to remove the aluminum layer from the MAX phase. Subsequent intercalation of nickel between the MXene layers was effectively performed using a hydrothermal method, as evidenced by the increase in interlayer spacing observed in the XRD results, where the (002) peak shifted from 8.89° to 6.79°. This corresponds to an increase in the d-spacing from 9.94 Å in MXene to 13.01 Å in MXN2, indicating that the MXN2 structure became significantly stronger and effectively resisted restacking. The intercalation of nickel also enhanced the specific surface area, with MXN2 reaching 35.27 $m^2$ $g^{-1}$ compared to MXene (3.96 $m^2$ $g^{-1}$) and MAX (1.1 $m^2$ $g^{-1}$), providing more accessible active sites for electrochemical reactions. Electrochemical characterization further demonstrated the superior performance of MXN2. In a 3-electrode system, MXN2 exhibited a high specific capacitance of 118.9 F $g^{-1}$ at 2 mV $s^{-1}$, while in a 2-electrode symmetric coin cell configuration, it achieved 60.03 F $g^{-1}$ at a current density of 0.1 A $g^{-1}$. The material delivered an energy density of 6.48 Wh $kg^{-1}$ and a power density of 176.72 W $kg^{-1}$, along with excellent cycling stability, retaining 97.47% of its capacitance after 1,000 cycles. Electrochemical impedance spectroscopy (EIS) results confirmed reduced resistances, with MXN2 showing $R_S$ of 4.55 Ω and $R_{CT}$ of 1.04 Ω, significantly lower than those of pristine MXene ($R_S$ = 4.7 Ω, $R_{CT}$ = 5.22 Ω). In summary, nickel intercalation not only increased the interlayer spacing and prevented restacking but also enhanced the surface area, electrochemical performance, and stability of MXene. These findings highlight MXN2 as a highly promising electrode material for high-stability, anti-restacking hybrid supercapacitors, offering substantial potential for next-generation energy storage applications.

## Acknowledgements

This research was funded by the national competitive grant from the Ministry of Research and National Research Board of Riset Kolaborasi Indonesia 2023 under contract No 13.5.4/UN32. 20/LT/ 2023.

## Declaration of generative AI in scientific writing

ChatGPT (OpenAI, GPT-4) was employed exclusively for language refinement and grammatical correction to ensure coherence of the manuscript. The AI tool was not used for content creation or data interpretation. The authors are fully responsible for the contents presented in this work.

## CRediT author statement

**Muhamad Subhan Septian:** Methodology, Data curation, Formal analysis, Investigation, Writing - original draft, Writing - review & editing; **Ishmah Luthfiyah:** Design-Visual graph, Data curation, Formal analysis, Investigation, Writing - review & editing; **Markus Diantoro:** Conceptualization, Resources, Supervision; **Worawat Meevasana:** Validation; **Agus Purwanto:** Validation; **Agus Subagio:** Validation; **Harith Ahmad:** Conceptualization; **Nida Usholihah**: Investigation

**References**


[1] IEA. Renewables 2023: Analysis and forecast to 2028, Available at: www.iea.org, accessed July 2025.

[2] L Yu and GZ Chen. Supercapatteries as high-performance electrochemical energy storage devices. *Electrochemical Energy Reviews* 2020; **3(2)**, 271-285.

[3] WK Wardani, NLW Septiani, SW Himmah, I Hamidah, M Diantoro, A Rusydi, H Abdullah and B Yuliarto. Layered nickel cobalt hydrogen phosphate for high performance of supercapattery electrode. *Journal of Materials Science: Materials in Electronics* 2024; **35(16)**, 1108.

[4] M Diantoro, I Istiqomah, OPD Lestari, Y Al Fath, Y Yudyanto, CI Yogihati, M Munasir, DH Kusumawati and ZB Aspanut. A comprehensive study of binder polymer for supercapattery electrode based on activated carbon and nickel-silicon composite. *Materials Science for Energy Technologies* 2023; **6**, 368-381.

[5] PS Dhapola, M Karakoti, S Kumar, VD Punetha, M Matiyani, NA Masmali, M Diantoro, SV Savilov and PK Singh. Environment-friendly approach for synthesis of promising porous carbon: Empowering supercapacitors for a sustainable future. *Materials Advances* 2024; **5(6)**, 2430-2440.

[6] MM Diantoro, I Istiqomah, YA Fath, N Nasikhudin, Y Alias and W Meevasana. Potential of $MnO_2$-based composite and numerous morphological for enhancing supercapacitors performance. *International Journal of Applied Ceramic Technology* 2023; **20(4)**, 2077-2098.

[7] P Forouzandeh and SC Pillai. MXenes-based nanocomposites for supercapacitor applications. *Current Opinion in Chemical Engineering* 2021; **33**, 100710.

[8] D Zhang, L Li, J Deng, S Guo, H Pang, J Lu, D Xia and X Ji. A new type of zinc ion hybrid supercapacitor based on 2D materials. *Nanoscale* 2021; **13(25)**, 11004-11016.

[9] SS Kumar, D Kang, H Hong, MA Rehman, Y Lee, N Lee and Y Seo. Effect of $Ti_3C_2T$: XMXenes etched at elevated temperatures using concentrated acid on binder-free supercapacitors. *RSC Advances* 2020; **10(68)**, 41837-41845.

[10] S Zhang, H Ying, P Huang, T Yang and WQ Han. Hierarchical utilization of raw $Ti_3C_2T_x$ MXene for fast preparation of various $Ti_3C_2T_x$ MXene derivatives. *Nano Research* 2022; **15(3)**, 2746-2755.

[11] N Xue, X Li, M Zhang, L Han, Y Liu and X Tao. Chemical-combined ball-milling synthesis of fluorine-free porous MXene for high-performance lithium ion batteries. *ACS Applied Energy Materials* 2020; **3(10)**, 10234-10241.

[12] BD Sankar, S Sekar, S Sathish, S Dhanasekaran, R Nirmala, DY Kim, Y Lee, S Lee and R Navamathavan. Recent advancements in MXene with 2-dimensional transition metal chalcogenides/oxides nanocomposites for supercapacitor application - A topical review. *Journal of Alloys and Compounds* 2024; **978**, 173481.

[13] K Zhang, G Ying, L Liu, F Ma, L Su, C Zhang, D Wu, X Wang and Y Zhou. Three-dimensional porous $Ti_3C_2T_x$-NiO composite electrodes with enhanced electrochemical performance for supercapacitors. *Materials* 2019; **12(1)**, 188.

[14] Z Li, M Jiang, F Wu, L Wu, X Zhang and L Li. Synergistic in-situ intercalation and surface modification strategy for $Ti_3C_2T_x$ MXene-based supercapacitors with enhanced electrochemical energy storage. *Journal of Energy Storage* 2023; **84**, 110772.

[15]P Das, TK Mondal, S Bera, S Das, HL Hsu, YK Su and SK Saha. Facile in-situ growth of spore-like silica on layered MXene sheets for potential application in Supercapacitor. *Electrochim Acta* 2023; **465**, 142983.

[16] G Lu, X Xing, J Zhang, X Xu, X Zhang, H Liu, J Fan and B Zhang. Rational design of cobalt ion chelated quasi-monolayer Ti3C2Tx MXene with abundant surface loading for high-performance asymmetric supercapacitor. *Colloids and Surfaces A: Physicochemical and Engineering Aspects* 2023; **671**, 131694.

[17] M Pogorielov, K Smyrnova, S Kyrylenko, O Gogotsi, V Zahorodna and A Pogrebnjak. Mxenes - a new class of 2-dimensional materials: Structure, properties and potential applications. *Nanomaterials* 2021; **11(12)**, 3412.

[18] J Yu, N Fu, J Zhao, R Liu, F Li, Y Dua and Z Yang. High specific capacitance electrode material for supercapacitors based on resin-derived nitrogen-doped porous carbons. *ACS Omega* 2019; **4(14)**, 15904-15911.

[19] M Imran, R Khan, AM Afzal, MW Iqbal, S Mumtaz, MZ Iqbal, X Zhang, A Ali, MD Albaqami and S Mohammad. Designing high-performance hybrid supercapacitors and electrochemical sensors with carbon nanotube-embedded silver manganese sulfide@AC@NF composites. *Journal of Energy Storage* 2024; **96**, 112642.

[20] Y Li, W Zhang, X Li, H Kang, B Yang nad Z Li. Facile solvothermal synthesis of $Co_{1-x}S$@CNTs/AC nanocomposite as integrated electrode for high-performance hybrid supercapacitors. *Journal of Alloys and Compounds* 2003; **932**, 404-406.

[21] X Chen, H Ge, W Yang, J Liu and P Yang. Construction of high-performance solid-state asymmetric supercapacitor based on $Ti_3C_2T_x$ MXene/CuS positive electrode and $Fe_2O_3$@rGO negative electrode. *Journal of Energy Storage* 2003; **68**, 107700.

[22] P Nikhil, S Vasanth, N Ponpandian and C Viswanathan. Synthesis effect on surface functionalized $Ti_3C_2T_x$ MXene supported nickel oxide nanocomposites with enhanced specific capacity for supercapacitor application. *Journal of Energy Storage* 2023; **72**, 108414.

[23] P Kathiravan, K Thillaivelavan, G Viruthagiri and N Shanmugam. Investigations of thermal, structural, optical, morphological and magnetic properties of chemical precipitation synthesized NiO nanoparticles for optoelectronic applications. *Journal of the Indian Chemical Society* 2024; **101(7)**, 101171.

[24] R Miao, W Zeng and QI Gao. Hydrothermal synthesis of novel NiO nanoflowers assisted with CTAB and SDS respectively and their gas-sensing properties. *Materials Letters* 2016; **115**, 60-66.

[25] I Luthfiyah, A Al Ittikhad, T Suprayogi, Nasikhudin, M Diantoro, S Maensiri and EH Sujiono. The effect of concentration PVP on microstructure activated carbon mesoporous and it's potential of activated carbon mesoporous-CB symmetric supercapacitors. *AIP Conference Proceedings* 2023; **2687**, 050025

[26] M Diantoro, I Luthfiyah, H Wisodo, J Utomo and W Meevasana. Electrochemical performance of symmetric supercapacitor based on activated carbon biomass $TiO_2$ nanocomposites. *Journal of Physics: Conference Series* 2022; **2243(1)**, 012077.

[27] IM Sutjahja, J Aarts, AA Nugroho, M Diantoro, MO Tjia, AA Menovsky and JJM Franse. Doping and field effects on the lowest Kramers doublet splitting in $La_{1.6-x}Nd_{0.4}Sr_xCuO_{4-\delta}$ single crystal. *Physica C: Superconductivity* 2020; **392-396**, 207-212.

[28] I Luthfiyah, J Utomo, M Diantoro, N Mufti, T Suprayogi, Y Yudyanto and A Aripriharta. The effect of spincoating speed on ZnONR microstructure and it's potential of ZnONR/Aluminum foil electrodes symmetric supercapacitors. *Journal of Physics: Conference Series* 2020; **1595(1)**, 012001.

[29] I Luthfiyah, J Utomo, M Diantoro, N Mufti, T Suprayogi, Y Yudyanto and A Aripriharta. Investigating the $CoS_2$ Mass fraction enhancing performance supercapacitor for medium low consumption. *E3S Web of Conferences* 2024; **473**, 03003.

[30] M Diantoro, NIM Aturroifah, I Luthfiyah, J Utomo, I Hamidah, B Yuliarto, A Rusydi, S Maensiri and Meevasana. 3D-porous activated carbon morphological modification of Manihot esculenta tuber and Bambusa blumeana stem for high-power density supercapacitor: Biomass waste to sustainable energy. *Carbon Resources Conversion* 2025; **8(4)**, 100313.

[31] M Diantoro, NIM Aturroifah, J Utomo, I Luthfiyah, I Hamidah, B Yuliarto, A Rusydi, W Meevesana, S Maensiri and PK Singh. Optimizing sponge-like activated carbon from Manihot esculenta tubers for high-performance supercapacitors. *Arabian Journal of Chemistry* 2025; **18(1)**, 106068.

[32] M Diantoro, RR Maisyarah and I Luthfiyah. The effect of activation temperature of coal carbon on its electrochemical performance as symmetric supercapacitors. *AIP Conference Proceedings* 2025; **3197(1)**, 020008.

[33] Y Niu, P Luo, X Chen, J Song, X He, H Sun, Z Li, C Wang and J Jiang. MXene/VS4 self-supporting thin film electrode for zinc-ion flexible supercapacitors. *Chemical Engineering Journal* 2024; **493**, 152372.

[34] K Prajapat, U Mahajan, M Dhonde, K Sahu nad PM Shirage. Synthesis and characterization of $TiO_2$ nanoparticles: Unraveling the influence of copper doping on structural, surface morphology, and optical properties. *Chemical Physics Impact* 2024; **8**, 100607.

[35] N Dogra, S Gasso, A Sharma, KK Sharma and S Sharma. $TiO_2$ decorated MXene nanosheets for high-performance ammonia gas sensing at room-temperature. *Surfaces and Interfaces* 2024; **48**, 104290.

[36] A Sarycheva and Y Gogotsi. Raman spectroscopy analysis of the structure and surface chemistry of $Ti_3C_2T_x$ Mxene. *Chemistry of Materials* 2020; **32**, 104290.

[37] T Hu, J Wang, H Zhang, Z Li, M Hu and X Wang. Vibrational properties of $Ti_3C_2$ and $Ti_3C_2T_2$ (T = O, F, OH) monosheets by first-principles calculations: A comparative study. *Physical Chemistry Chemical Physics* 2015; **17(15)**, 9997-10003.

[38] AY Komariyah, I Luthfiyah, IV Albadi'ah, N Nasikhudin, W Meevasana and M Diantoro. Harnessing the role of carbon black: A new frontier for energy-density supercapacitor electrodes. *Journal of Mechanical Engineering Science and Technology* 2025; **9(1)**, 268.

[39] M Diantoro, RR Maisyarah and I Luthfiyah. The effect of activation temperature of coal carbon on its electrochemical performance as symmetric supercapacitors. *AIP Conference Proceedings* 2025; **3197(1)**, 020008.

[40] PC Ogugua, H Su and E Wang. Synergistic blending of biomass, sewage sludge, and coal for enhanced bioenergy production: Exploring residue combinations and optimizing thermal conversion parameters. *Journal of Environmental Management* 2024; **352**, 120035.

[41] M Hu, L Chen, Y Jing, Y Zhu, J Dai, A Meng, C Sun, J Jia and Z Li. Intensifying electrochemical activity of Ti3C2Tx MXene via customized interlayer structure and surface chemistry. *Molecules* 2023; **28(15)**, 5776.

[42] HH Hegazy, AM Afzal, ER Shaaban, MW Iqbal, S Muhammad and AA Alahmari. Synthesis of MXene and design the high-performance energy harvesting devices with multifunctional applications. *Ceramics Internasional* 2023; **49(2)**, 1710-1719.

[43] Z Lin, D Barbara, PL Taberna, KL Van Aken, B Anasori, Y Gogotsi and P Simon. Capacitance of Ti3C2Tx MXene in ionic liquid electrolyte. *Journal of Power Sources* 2017; **326**, 575-579.

[44] S Kumar, MA Rehman, S Lee, M Kim, H Hong, JY Park and Y Seo. Supercapacitors based on $Ti_3C_2T_x$ MXene extracted from supernatant and current collectors passivated by CVD-graphene. *Scientific Reports* 2021; **11(1)**, 649.

[45] BK Deka, A Hazarika, GH Kang, YJ Hwang, AP Jaiswal, D Chan Kim, YB Park and HW Park. 3D printed structural supercapacitor with MXene-N @ Zn-Co selenide nanowire-based woven carbon fiber electrodes. *ACS Energy Letters* 2023; **3(2)**, 963-971.

[46] VSH Priyaa, R Saravanathamizhan and N Balasubramanian. Preparation of biomass based carbon for elctrochemical energy storage application. *Journal of Electrochemical Science and Technology* 2019; **10(2)**, 159-169.

[47] A Shah, S Senapati, HCA Murthy, LR Singh and M Mahato. Supercapacitor performance of NiO, NiO-MWCNT, and NiO-Fe-MWCNT composites. *ACS Omega* 2023; **37(8)**, 33380-33391.

[48] Y Wang, N Chen, Y Liu, X Zhou, B Pu, Y Qing, M Zhang, X Jiang, J Huang, Q Tang, B Zhou and W Yang. MXene/graphdiyne nanotube composite films for Free-Standing and flexible Solid-State supercapacitor. 2022; **450(4)**, 138398.

[49] A El-Ghazaly, J Halim, B Ahmed, AS Etman and J Rosen. Exploring the electrochemical behavior of Mo1.33CTz MXene in aqueous sulfates electrolytes: Effect of intercalating cations on the stored charge. *Journal of Power Sources* 2022; **531**, 231302.

[50] JJ Zhu, A Hemesh, JJ Biendicho, L Martinez-Soria, D Rueda-Garcia, JR Morante, B Ballesteros and P Gomez-Romero. Rational design of

MXene/activated carbon/polyoxometalate triple hybrid electrodes with enhanced capacitance for organic-electrolyte supercapacitors. *Journal of Colloid and Interface Science* 2022; **623**, 947-961.

[51] Y Wei, M Zheng, W Luo, B Dai, J Ren, M Ma, T Li and Y Ma. All pseudocapacitive MXene-MnO2 flexible asymmetric supercapacitor. *Journal of Energy Storage* 2021; **45**, 103725.

[52] T Arun, A Mohanty, A Rosenkranz, B Wang, J Yu, MJ Morel, R Udayabhaskar, SA Hevia, A Akbari-Fakhrabadi, RV Mangalaraja and A Ramadoss. Role of electrolytes on the electrochemical characteristics of Fe3O4/MXene/RGO composites for supercapacitor applications. *Electrochimica Acta* 2021; **367**, 137473.

[53] L Yang, W Zheng, P Zhang, J Chen, WB Tian, YM Zhang and ZM Sun. MXene/CNTs films prepared by electrophoretic deposition for supercapacitor electrodes. *Journal of Electroanalytical Chemistry* 2018; **830-831**, 1-6.

[54] X Li, Z Lin, Y Wei, W Luo, J Ding, T Li and Y Ma. MXene-$MnO_2$-CoNi layered double hydroxides// activated carbon flexible asymmetric supercapacitor. 2022; **55**, 46-48.

[55] M Pathak, SR Polaki and CS Rout. High performance asymmetric supercapacitors based on Ti3C2Tx MXene and electrodeposited spinel $NiCo_2S_4$ nanostructures. *RSC Advances* 2022; **22**, 10788-10799.